energies

MDPI

Article

Thermal Analysis of Parabolic and Fresnel Linear Solar Collectors Using Compressed Gases as Heat Transfer Fluid in CSP Plants

Roberto Grena [1], Michela Lanchi [1,*], Marco Frangella [2], Vittorio Ferraro [2], Valerio Marinelli [2] and Marco D'Auria [1]

[1] ENEA—Italian National Agency for New Technologies, Energy and Sustainable Economic Development, 00123 Rome, Italy; roberto.grena@enea.it (R.G.); marco.dauria@enea.it (M.D.)
[2] Department of Mechanical Energy and Management Engineering, University of Calabria, 87036 Rende, Italy; frangellamarco@gmail.com (M.F.); vittorio.ferraro@unical.it (V.F.); valerio.marinelli@unical.it (V.M.)
* Correspondence: michela.lanchi@enea.it

Abstract: This study introduces the use of compressed air as a heat transfer fluid in small-scale, concentrated linear solar collector technology, evaluating its possible advantages over traditional fluids. This work assumes the adoption of readily available components for both linear parabolic trough and Fresnel collectors and the coupling of the solar field with Brayton cycles for power generation. The aim is to provide a theoretical analysis of the applicability of this novel solar plant configuration for small-scale electricity generation. Firstly, a lumped thermal model was developed in a MatLab® (v. 2023a) environment to assess the thermal performance of a PT collector with an evacuated receiver tube. This model was then modified to describe the performance of a Fresnel collector. The resulting optical–thermal model was validated through literature data and appears to provide realistic estimates of temperature distribution along the entire collector length, including both the receiver tube surface and the Fresnel collector's secondary concentrator. The analysis shows a high thermal efficiency for both Fresnel and parabolic collectors, with average values above 0.9 (in different wind conditions). Th5s study also shows that the glass covering of the Fresnel evacuated receiver, under the conditions considered (solar field outlet temperature: 550 °C), reaches significant temperatures (above 300 °C). Furthermore, due to the presence of the secondary reflector, the temperature difference between the upper and the lower part of the glass envelope can be very high, well above 100 °C in the final part of the collector string. Differently, in the case of PTs, this temperature difference is quite limited (below 30 °C).

Keywords: Concentrated Solar Power (CSP) technology; parabolic trough collectors; Fresnel collectors; solar receiver model; gaseous heat transfer fluid

Citation: Grena, R.; Lanchi, M.; Frangella, M.; Ferraro, V.; Marinelli, V.; D'Auria, M. Thermal Analysis of Parabolic and Fresnel Linear Solar Collectors Using Compressed Gases as Heat Transfer Fluid in CSP Plants. *Energies* **2024**, *17*, 3880. https://doi.org/10.3390/en17163880

Academic Editor: Luigi Vesce

Received: 14 June 2024
Revised: 23 July 2024
Accepted: 31 July 2024
Published: 6 August 2024

1. Introduction

Concentrated Solar Power (CSP) technology is widely considered as a key accelerator for the transition to a fully decarbonized energy and industrial system. Indeed, thanks to the thermal energy storage, CSP is inherently flexible, able to generate electricity/heat on demand and therefore able to effectively stabilize energy flows in distribution networks affected by a high level of non-programmable renewable sources [1]. In the upcoming decades, a substantial increase in the share of energy produced by CSP is expected. According to the International Energy Agency's high renewable use scenario, by 2050 it will cover more than 10% of the global primary energy requirement [2]. ENEA, the Italian National Agency for New Technologies, Energy and Sustainable Economic Development, has been active in the CSP sector since 2000. Its research efforts have been mainly focused on the development of new materials, innovative components and low-cost operational strategies for concentrated solar linear collectors. Notably, since 2001, the Agency has

pursued groundbreaking research on Parabolic Trough (PT) plants, replacing diathermic oils, the conventionally used heat transfer fluid (HTF), with molten salt mixtures. This approach aims to achieve very high solar field operating temperatures (550 °C, in place of 400 °C), allowing to increase the efficiency of thermal-to-electricity conversion and reducing the environmental impact of conventional HTFs.

This innovative technology's development has unfolded over several years, involving both in-depth research on individual components (particularly receiver tubes using a patented spectrally selective coating, stable up to 600 °C [3]) and the construction of a full-scale test facility at ENEA's Casaccia Research Centre. Furthermore, two demonstration plants were realized (Figure 1) to test and characterize plant components dealing with molten salts: the Archimede plant [4] (co-developed with ENEL in Priolo Gargallo, Italy) and the MATS plant [5,6] (built in Egypt as part of the European MATS project). In addition to the main research line on PT technology, the use of the same molten salt mixture (the binary "solar" salt mixture) as HTF for linear Fresnel receivers (LFRs) has also been explored [7]. In this respect, it is worth noticing that a dedicated test facility at the Casaccia Research Center has been recently realized for materials/components testing, and that, in the last years, commercial plants based on this Fresnel/molten salts technology have been built in Sicily, Partanna and Stromboli (MS-LFR CSP Projects [8,9]).

(**a**) (**b**)

Figure 1. PCS Test Facility at the ENEA Casaccia Research Center of Rome (**a**); MATS demonstrative plant (Borg El Arab, Egypt) (**b**).

While large-scale CSP plants (above 50 MWe) are being developed and installed all over the world, benefitting from the cost reduction through the economy of scale (e.g., CSNP Urat and Lanzhou Dacheng Dunhuang in China, and the Shagaya CSP Project in Kuwait [9]), a parallel and promising market segment for distributed polygeneration is emerging. This market aligns perfectly with the social and industrial requirements of Euro-Mediterranean countries, which have limited areas to be destined for solar energy harvesting and a very heterogeneous energy demand. Therefore, new solutions that can be easily integrated into industrial/urbanized environments (building rooftops, abandoned areas, car parks, etc.) must be developed.

However, this shift from centralized to distributed generation requires suitable HTFs for compact solar systems that are easily managed, safely operated and environmentally friendly. Currently, CSP plants, dominated by linear concentrator technology, rely on thermal oils for large-scale applications [10]. As mentioned above, prototypes and demonstration plants, which use molten salts mixtures as HTFs, have been recently realized [11]. Both these options seem unsuitable for use in small-scale plants, for different reasons. Diathermic oils pose a challenge due to their flammability and environmental impact. Solar salt mixtures are hindered by a high freezing point (around 240 °C), which significantly increases operational complexity and costs. To maintain the solar field above this temperature, constant circulation, even at night, is required, leading to daily heat losses of 3–4% of captured solar thermal energy. Moreover, these HTFs are subjected to thermal degradation (above 400 °C and 600 °C for thermal oils and molten salts, respectively [12]). All these aspects require a complex management of the HTF circulation, with the realization of complex control systems and the implementation of risk management structures that

are affordable for large plants but can be problematic for small-to-medium scale, modular plants. Therefore, testing new HTFs with high thermal stability, non-flammability and non-polluting properties, along with resistance to freezing, is essential. This would pave the way for cost-effective, small-scale, distributed solar applications, where minimizing operational and maintenance costs is of paramount importance.

Among the different alternatives that have been proposed as HTFs, the application of compressed gases remains substantially underexplored [13]. The present study aims to fill this gap by analyzing the technical viability of compressed air as HTF in small-scale, linear solar collectors (PT and LFR) as a substitute for current options. Compressed gases offer the potential advantage of extended operation temperature ranges, as well as a very limited environmental impact. Furthermore, compressed gases can be directly processed in Brayton cycle power units, which are suitable for small-scale, flexible electricity generation, and can be easily integrated with conventional combustors, fed by fuels/biofuels, for 24 h production.

Specifically, the possibility of utilizing readily available components for both parabolic trough and Fresnel collectors, adapting them to operate with pressurized gases, has been investigated. The analysis was focused on air as the most cost-effective and readily available option, and a simplified thermal model (lumped model) for the description of linear collector behavior was developed. This model was applied to assess the thermal efficiency of the solar field and identify potential limitations at the component level, considering both mechanical and thermal factors.

The objective is to theoretically verify if a combination of existing concentrating technologies and gaseous HTF can be a viable way to realize small-scale, flexible plants. This paper, in particular, presents the optical and thermal analysis of both PT and LFR concentrators, arriving to the calculation of optical and thermal efficiencies, and to the definition of some critical aspects that could hinder the applicability of the technology (e.g., the temperature of the components or the pressure of the gas).

Sections 2 and 3 of the paper describe the adopted models for a PT and a LFR, respectively, presenting both the optical and thermal models developed. Particularly, the lumped thermal model considers the receiver tube divided into discrete sections, and each section was analyzed under the assumptions of uniform properties and steady-state conditions. Sections 4 and 5 present relevant results of the simulations for PT and LFR, respectively. Results are then discussed and commented upon in Section 6, with a special focus on the possible critical points for the applicability of the technology.

2. Parabolic Trough Collectors Modelling

Parabolic trough collectors concentrate solar radiation onto a focal line, where an absorber tube encased within an evacuated glass envelope is positioned (Figure 2). This absorber tube features a special spectrally selective coating with high solar absorptivity and low thermal emissivity (typically based on cermets).

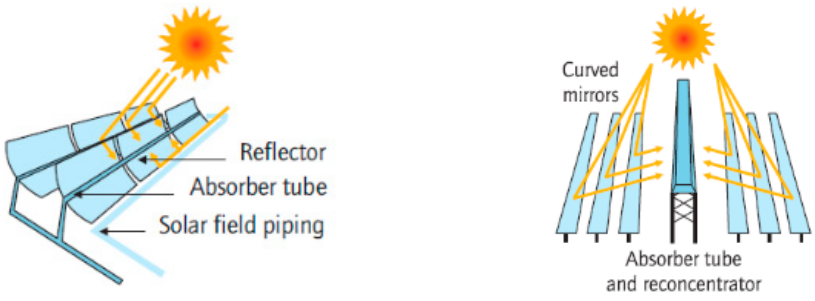

(**a**) (**b**)

Figure 2. Parabolic trough collector (**a**); linear Fresnel collector (**b**) from [14].

The optical model here developed calculates the angular distribution of radiation absorbed by both the cermet layer and the glass envelope. This calculation helps to validate the accuracy of the simplified thermal model and provides essential input data (absorbed radiation) for the thermal analysis.

The PT thermal model here developed is based on a two-step discretization process. First, the collector is divided longitudinally into segments matching the number of receiver tubes. Each receiver tube is then radially divided into two halves (upper and lower half), creating a basic radial discretization.

2.1. Optical Model

The optical simulation of the parabolic trough collector utilizes the ray-tracing software SimulTrough (v. 1.0) described in [15]. The software calculates the distribution of radiation absorbed by both the receiver tube and the glass envelope. The software assumes a uniform distribution of solar beams (groups of rays reproducing the angular distribution of the sun's radiation) striking the collector's aperture. These rays are then tracked through the system, following their path as they undergo reflections and refractions until their energy becomes negligible. Rays that refract, like those at the glass surface, generate secondary rays that are also tracked recursively.

The software offers the possibility to incorporate common defects that can influence radiation distribution, such as tracking errors, receiver defocusing, random mirror slope errors and large-scale mirror deformations.

As the primary focus of this work is analyzing the thermal performance of the collector loop, the relative amount of radiation absorbed by the "lower half" (facing the collector) compared to the "upper half" (facing the sky) was the output of the optical simulation.

2.2. Thermal Model

The thermal model is based on Forristal's approach [16].

The model deals with the absorber tube and the glass envelope as separate sections. The thermal power balance for the absorber tube can be expressed as follows:

$$\dot{Q}_{sol,abs} = \dot{Q}_{HTF} + \dot{Q}^{u}_{lost} + \dot{Q}^{l}_{lost}, \tag{1}$$

The following relations were used to calculate the power absorbed by the HTF (see Nomenclature Table):

- Conservation of mass: $\rho u = const$;
- First law of thermodynamics: $\dot{Q}_{HTF} = \Delta\dot{H} + \Delta\dot{E}_k$;
- Conservation of mechanical energy: $\int_{in}^{out} v dp + \frac{u_{out}^2}{2} - \frac{u_{in}^2}{2} + Y = 0$;
- Convection heat transfer from inner surfaces of the absorber tube to the HTF, according to Newton's law of cooling: $\dot{Q}_{HTF} = h_{conv} d_{abs} \pi$, with

$$h_{conv} = \frac{k_{HTF}}{d_{abs}} Nu_{HTF} \tag{2}$$

and, in accordance with the Dittus–Boelter correlation,

$$Nu_{HTF} = 0.023 Re_{HTF}^{0.8} Pr_{HTF}^{0.4} \tag{3}$$

$$Re_{HTF} = \frac{\rho_{HTF} u_{HTF} d_{abs,i}}{\mu_{HTF}} \tag{4}$$

$$Pr_{HTF} = \frac{c_{p,HTF} \mu_{HTF}}{k_{HTF}} \tag{5}$$

With reference to Figure 3, the following equations were considered for the heat transfer model of a PT receiver:

$$\dot{Q}_{2-1,conv} = \dot{Q}_{3-2,cond} \tag{6}$$

$$\dot{Q}_{3,sol,abs} = \dot{Q}_{3-2,cond} + \dot{Q}_{3-4,rad} \tag{7}$$

$$\dot{Q}_{3-4,rad} = \dot{Q}_{4-5,cond} \tag{8}$$

$$\dot{Q}_{4-5,cond} + \dot{Q}_{5,sol,abs} = \dot{Q}_{5-a,conv} + \dot{Q}_{5-a,rad} \tag{9}$$

$$\dot{Q}_{6-1,conv} = \dot{Q}_{6-7,cond} \tag{10}$$

$$\dot{Q}_{7,sol,abs} = \dot{Q}_{7-6,cond} + \dot{Q}_{7-8,rad} \tag{11}$$

$$\dot{Q}_{7-8,rad} = \dot{Q}_{8-9,cond} \tag{12}$$

$$\dot{Q}_{8-9,cond} + \dot{Q}_{9,sol,abs} = \dot{Q}_{9-a,conv} + \dot{Q}_{9-a,rad} \tag{13}$$

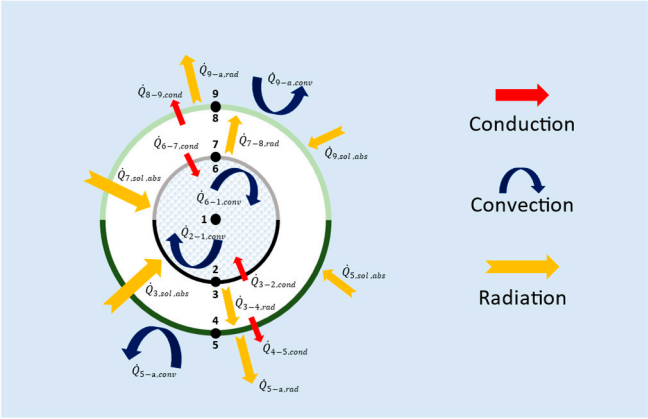

Figure 3. Schematization of heat transfer mechanisms along a generic axial section of the PT.

Regarding the convective heat losses from the glass envelope to the surrounding environment, in the present study a methodology for its evaluation was developed, considering both natural and forced convection scenarios.

In the case of natural convection, the Nusselt number for both the lower and upper halves of the envelope was estimated using the correlation developed by Churchill and Chu [17]:

(a) Computation of the convective heat transfer coefficient between the lower part of the glass envelope and the external environment in non-windy cases

$$h_{5-a,conv} = \frac{k_{air,5-a}}{d_5} Nu_{air,5-a} \tag{14}$$

$$Nu_{air,5-a} = \left\{ 0.60 + 0.387 Ra_{air,5-a}^{\frac{1}{6}} \left[1 + \left(0.559 Pr_{air,5-a}^{-1} \right)^{\frac{9}{16}} \right]^{-\frac{8}{27}} \right\}^2 \tag{15}$$

$$Ra_{air,5-a} = Gr_{air,5-a} \cdot Pr_{air,5-a} \tag{16}$$

$$Gr_{air,5-a} = \frac{g \rho_{air,5-a} d_5^3 \alpha_{air,5-a} (T_5 - T_a)}{\mu_{air,5-a}^2} \tag{17}$$

$$Pr_{air,5-a} = \frac{c_{p,air,5-a} \mu_{air,5-a}}{k_{air,5-a}} \tag{18}$$

(b) Computation of the convective heat transfer coefficient between the upper part of the glass envelope and the external environment in non-windy cases

$$h_{9-a,conv} = \frac{k_{air,9-a}}{d_9} Nu_{air,9-a} \tag{19}$$

$$Nu_{air,9-a} = \left\{ 0.60 + 0.387 Ra_{air,9-a}^{\frac{1}{6}} \left[1 + \left(0.559 Pr_{air,9-a}^{-1} \right)^{\frac{9}{16}} \right]^{-\frac{8}{27}} \right\}^2 \tag{20}$$

$$Ra_{air,9-a} = Gr_{air,9-a} \cdot Pr_{air,9-a} \tag{21}$$

$$Gr_{air,9-a} = \frac{g \rho_{air,9-a} d_9^3 \alpha_{air,9-a} (T_9 - T_a)}{\mu_{air,9-a}^2} \tag{22}$$

$$Pr_{air,9-a} = \frac{c_{p,air,9-a} \mu_{air,9-a}}{k_{air,9-a}} \tag{23}$$

In windy conditions, the Nusselt number for both the lower and upper halves was evaluated using the correlation developed by Zukauskas [18]:

(a) Computation of the convective heat transfer coefficient between the lower part of the glass envelope and the external environment in windy cases

$$h_{5-a,conv} = \frac{k_{air,5-a}}{d_5} Nu_{air,5-a} \tag{24}$$

$$Nu_{air,5-a} = 0.26 Re_{air,5-a}^{0.6} Pr_{air,a} \left(\frac{Pr_{air,a}}{Pr_{air,5}} \right)^{0.25} \tag{25}$$

$$Re_{air,5-a} = \frac{d_5 u_{wind} \rho_{air,5-a}}{\mu_{air,5-a}} \tag{26}$$

$$Pr_{air,5} = \frac{c_{p,air,5} \mu_{air,5}}{k_{air,5}} \tag{27}$$

$$Pr_{air,a} = \frac{c_{p,air,a} \mu_{air,a}}{k_{air,a}} \tag{28}$$

$$h_{9-a,conv} = \frac{k_{air,9-a}}{d_9} Nu_{air,9-a} \tag{29}$$

(b) Computation of the convective heat transfer coefficient between the upper part of the glass envelope and the external environment in windy cases

$$Nu_{air,9-a} = 0.26 Re_{air,9-a}^{0.6} Pr_{air,a} \left(\frac{Pr_{air,a}}{Pr_{air,9}} \right)^{0.25} \tag{30}$$

$$Re_{air,9-a} = \frac{d_9 u_{wind} \rho_{air,9-a}}{\mu_{air,5-a}} \tag{31}$$

$$Pr_{air,9} = \frac{c_{p,air,9} \mu_{air,9}}{k_{air,9}} \tag{32}$$

$$Pr_{air,a} = \frac{c_{p,air,a} \mu_{air,a}}{k_{air,a}} \tag{33}$$

Equations (1)–(33) were implemented in a lumped thermal model developed in a MatLab® (v. 2023a) environment by discretizing the collector loop at each receiver tube. The differential equations for the temperatures and pressure along the collector loop were solved using the forward Euler method, and the correct final temperature was obtained by tuning the initial conditions (shooting method). This model allowed the estimation of the

thermal efficiency, the temperature profiles and the pressure drop along the loop of a linear parabolic collector equipped with an evacuated tube receiver.

3. Linear Fresnel Collector Modelling

Differently from parabolic troughs, Fresnel collectors consist of multiple mirror strips. These strips rotate individually at ground level, concentrating reflected sunlight onto a fixed, elevated absorber. Additionally, in this case, the absorber is typically an evacuated tube, positioned within a secondary reflector (Figure 2). The secondary reflector redirects stray rays from each mirror towards the absorber, maximizing captured solar energy.

Like the PT, the thermal model of the LFR uses a two-step discretization process. Firstly, the collector was divided longitudinally into as many nodes as receiver tubes. Secondly, each receiver tube was further divided radially into two halves (upper and lower), creating a basic radial discretization.

3.1. Optical Model

An Octave software-based ray-tracing model was developed for the Fresnel collector. The model, with an accuracy not as high as the one of the PT, seems to effectively capture the key aspect for validating the thermal model, which is the ratio of absorbed radiation between the lower and upper halves of the receiver.

The primary simplification compared to the trough model is the omittance of the glass cover. Indeed, simulations showed minimal impact on ray trajectories due to the thin glass cover in the PT. Additionally, the absorbed radiation distribution on the glass could be reliably estimated by mirroring the receiver's distribution. Therefore, a bare tube simulation was used. The presence of glass was then addressed by the following:

- Reducing the absorber's radiation intensity based on the glass' overall transmittance.
- Introducing a volumetric source within the glass, representing overall absorbance and mirroring the receiver's angular radiation distribution.

The PT results confirmed that these approximations were suitable for calculating radiation fractions in the half-tubes.

The model also accounted for the radiation absorbed by the secondary reflector, a Compound Parabolic Concentrator (CPC), which is a significant factor in secondary receiver heating and overall thermal efficiency.

3.2. Thermal Model

The thermal model is based on Forristal's approach [16], and Equations (1)–(5), valid for the PT receiver tube, were also applied in this case. Conversely, the thermal model for the Fresnel receiver differs from the PT's one: indeed, the secondary reflector in the thermal model of the Fresnel receiver is an additional element to the heat exchange process. Furthermore, specific heat balance equations for convective heat exchange are required to describe windy or non-windy conditions. As illustrated in Figure 4, windy conditions promote direct convective heat exchange between the lower half of the glass envelope and the surrounding environment ($\dot{Q}_{5-a,conv}$, represented as a white-filled arrow in Figure 4) and Equations (43) and (44) can be applied. Differently, under non-windy (i.e., still air) conditions, the lower half of the glass envelope primarily transfers heat via convection to the secondary reflector ($\dot{Q}_{5-10,conv}$, represented as striped arrow in Figure 4), and Equations (41) and (42) were applied.

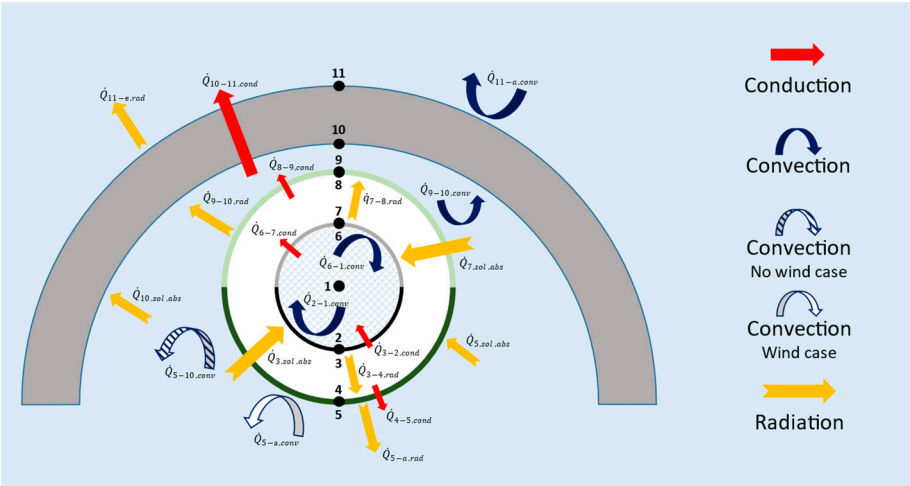

Figure 4. Schematization of heat transfer mechanisms along a generic axial section of a LFR.

The following equations can be written for the heat transfer model of a Fresnel receiver, referring to Figure 4:

$$\dot{Q}_{2-1,conv} = \dot{Q}_{3-2,cond} \tag{34}$$

$$\dot{Q}_{3,sol,abs} = \dot{Q}_{3-2,cond} + \dot{Q}_{3-4,rad} \tag{35}$$

$$\dot{Q}_{3-4,rad} = \dot{Q}_{4-5,cond} \tag{36}$$

$$\dot{Q}_{6-1,conv} = \dot{Q}_{6-7,cond} \tag{37}$$

$$\dot{Q}_{7-8,rad} = \dot{Q}_{8-9,cond} \tag{38}$$

$$\dot{Q}_{8-9,cond} + \dot{Q}_{9,sol,abs} = \dot{Q}_{9-10,conv} + \dot{Q}_{9-10,rad} \tag{39}$$

$$\dot{Q}_{10-11,cond} = \dot{Q}_{11-a,conv} + \dot{Q}_{11-a,rad} \tag{40}$$

In the absence of wind, Equations (41) and (42) must also be considered:

$$\dot{Q}_{4-5,cond} + \dot{Q}_{5,sol,abs} = \dot{Q}_{5-10,conv} + \dot{Q}_{5-a,rad} \tag{41}$$

$$\dot{Q}_{5-10,conv} + \dot{Q}_{9-10,conv} + \dot{Q}_{9-10,rad} + \dot{Q}_{10,sol,abs} = \dot{Q}_{10-11,cond} \tag{42}$$

For windy conditions, Equations (43) and (44) must be taken into account:

$$\dot{Q}_{4-5,cond} + \dot{Q}_{5,sol,abs} = \dot{Q}_{5-a,conv} + \dot{Q}_{5-a,rad} \tag{43}$$

$$\dot{Q}_{9-10,conv} + \dot{Q}_{9-10,rad} + \dot{Q}_{10,sol,abs} = \dot{Q}_{10-11,cond} \tag{44}$$

The presence of the CPC influences the convective heat losses from the glass envelope of a LFR to the surrounding environment.

Under still air conditions (natural convection), the convective heat transport within the receiver cavity was evaluated using Raithby and Hollands' correlation [19], calculated from the equivalent thermal conductivity. This correlation was proven effective in similar applications [20]. To determine the free convection heat loss from the back casing, the Churchill and Chu correlation [17] was assumed. Here, the back casing is approximated as a long, horizontal semi-cylinder.

The following formulas were used:

(a) Computation of the convective heat transfer coefficient between the lower part of the glass envelope and the external environment in non-windy cases

$$h_{5-10,conv} = \frac{k_{eq,5-10}}{\log\left(\frac{r_{10}}{r_5}\right) r_5} \tag{45}$$

$$\frac{k_{eq,5-10}}{k_{air,5-10}} = 0.386\left(\frac{Pr_{air,5-10}}{0.861 + Pr_{air,5-10}}\right)^{\frac{1}{4}} Ra_{5-10,Lc}^{\frac{1}{4}} \tag{46}$$

$$Ra_{5-10,Lc} = Gr_{5-10,Lc} \cdot Pr_{air,5-10} \tag{47}$$

$$Gr_{5-10,Lc} = \frac{g\rho_{air,5-10} L_{c,5-10}^3 \alpha_{air,5-10}(T_5 - T_{10})}{\mu_{air,5-10}^2} \tag{48}$$

$$L_{c,5-10} = \frac{2\left(ln\left(\frac{r_{10}}{r_5}\right)\right)^{\frac{4}{3}}}{\left(r_5^{-\frac{3}{5}} + r_{10}^{-\frac{3}{5}}\right)^{\frac{5}{3}}} \tag{49}$$

(b) Computation of the convective heat transfer coefficient between the upper part of the glass envelope and the external environment in non-windy cases

$$h_{9-10,conv} = \frac{k_{eq,9-10}}{log\left(\frac{r_{10}}{r_9}\right) r_9} \tag{50}$$

$$\frac{k_{eq,9-10}}{k_{air,9-10}} = 0.386\left(\frac{Pr_{air,9-10}}{0.861 + Pr_{air,9-10}}\right)^{\frac{1}{4}} Ra_{Lc}^{\frac{1}{4}} \tag{51}$$

$$Ra_{Lc} = Gr_{Lc} \cdot Pr \tag{52}$$

$$Gr_{9-10,Lc} = \frac{g\rho_{air,9-10} L_{c,9-10}^3 \alpha_{air,9-10}(T_9 - T_{10})}{\mu_{air,9-10}^2} \tag{53}$$

$$L_{c,9-10} = \frac{2\left(ln\left(\frac{r_{10}}{r_9}\right)\right)^{\frac{4}{3}}}{\left(r_9^{-\frac{3}{5}} + r_{10}^{-\frac{3}{5}}\right)^{\frac{5}{3}}} \tag{54}$$

(c) Computation of the convective heat transfer coefficient between the CPC back casing and the external environment in non-windy cases

$$h_{11-a,conv} = \frac{k_{air,11-a}}{d_{11}} Nu_{air,11-a} \tag{55}$$

$$Nu_{air,11-a} = \left\{0.60 + 0.387 Ra_{air,11-a}^{\frac{1}{6}}\left[1 + \left(0.559 Pr_{air,11-a}^{-1}\right)^{\frac{9}{16}}\right]^{-\frac{8}{27}}\right\}^2 \tag{56}$$

$$Ra_{air,11-a} = Gr_{air,11-a} \cdot Pr_{air,11-a} \tag{57}$$

$$Gr_{air,11-a} = \frac{g\rho_{air,11-a} d_{11}^3 \alpha_{air,11-a}(T_{11} - T_a)}{\mu_{air,11-a}^2} \tag{58}$$

$$Pr_{air,11-a} = \frac{c_{p,air,11-a}\mu_{air,11-a}}{k_{air,11-a}} \tag{59}$$

For windy conditions, the convective heat transfer coefficient and the Nusselt number between the glass envelope and the CPC were estimated using a correlation proposed by

Reddy et al. [21–23]: these correlations were derived by fitting the results of numerical simulations. The convective heat losses from the CPC to the surrounding environment were calculated using the Hilpert correlation [24]. The following relations were used:

(a) Computation of the convective heat transfer coefficient between the lower part of the glass envelope and the external environment in windy cases

$$h_{5-a,conv} = \frac{k_{air.5-a}}{r_{10}} Nu_{air,5-a} \tag{60}$$

$$Nu_{5-a} = 8.424\left(\frac{T_5}{T_a}\right)^{-0.567}\left(\frac{r_5}{r_{10}}\right)^{-0.573}{\varepsilon_5}^{-0.097}\left(\frac{Gr_{5-a,Lc}}{1+Re^2_{air,5-a}}\right)^{-0.045} \tag{61}$$

$$Re_{air,5-a} = \frac{d_5 u_{wind}\rho_{air,5-a}}{\mu_{air,5-a}} \tag{62}$$

$$Gr_{5-a,Lc} = \frac{g\rho_{air,5-a}L_c^3\alpha_{air,5-a}(T_5 - T_a)}{\mu^2} \tag{63}$$

$$L_c = \frac{2\left(ln\left(\frac{r_{10}}{r_5}\right)\right)^{\frac{4}{3}}}{\left(r_5^{-\frac{3}{5}} + r_{10}^{-\frac{3}{5}}\right)^{\frac{5}{3}}} \tag{64}$$

(b) Computation of the convective heat transfer coefficient between the upper part of the glass envelope and the external environment in windy cases

$$h_{9-10,conv} = \frac{k_{air,9-10}}{r_{10}} Nu_{air,9-10} \tag{65}$$

$$Nu_{9-10} = 8.424\left(\frac{T_9}{T_a}\right)^{-0.567}\left(\frac{r_9}{r_{10}}\right)^{-0.573}{\varepsilon_9}^{-0.097}\left(\frac{Gr_{9-a,Lc}}{1+Re^2_{air,a}}\right)^{-0.045} \tag{66}$$

$$Re_{air,9-a} = \frac{d_9 u_{wind}\rho_{air,9-a}}{\mu_{air,9-a}} \tag{67}$$

$$Gr_{9-a,Lc} = \frac{g\rho_{air,9-a}L_c^3\alpha_{air,9-a}(T_9 - T_a)}{\mu^2} \tag{68}$$

$$L_c = \frac{2\left(ln\left(\frac{r_{10}}{r_9}\right)\right)^{\frac{4}{3}}}{\left(r_9^{-\frac{3}{5}} + r_{10}^{-\frac{3}{5}}\right)^{\frac{5}{3}}} \tag{69}$$

(c) Computation of the convective heat transfer coefficient between the CPC back casing and the external environment in windy cases

$$h_{11-a,conv} = \frac{k_{air,11-a}}{d_{11}} Nu_{air,11-a} \tag{70}$$

$$Nu_{air,11-a} = 0.193 \cdot Re^{0.618}_{air,\ 11-a} \cdot Pr^{1/3}_{air,11-a} \tag{71}$$

$$Re_{air,11-a} = \frac{d_9 u_{wind}\rho_{air,11-a}}{\mu_{air,11-a}} \tag{72}$$

$$Pr_{air,11-a} = \frac{c_{p,air,11-a}\mu_{air,11-a}}{k_{air,11-a}} \tag{73}$$

For the Fresnel receiver, Equations (1)–(5), in combination with Equations (34)–(73), were implemented in a lumped thermal model developed in a MatLab® environment by discretizing the collector loop at each receiver tube. The differential equations for temperatures and pressure along the collector loop were solved using the forward Euler method, and the correct final temperature was obtained by tuning the initial conditions (shooting method).

4. Parabolic Trough Models Application for Thermal Performance Evaluation

To analyze the performance of a linear parabolic trough collector, the following geometrical and configurational parameters (Tables 1 and 2) were assumed. The analysis was limited to a maximum absorber tube temperature of 600 °C, as exceeding this temperature can degrade the selective coating here considered (ENEA's Cermet, [3]), according to experimental observations. It is important to note that this collector is a commercial design specifically intended for incompressible heat transfer fluids (diathermic oils or salts) and not for compressed gases.

Table 1. Geometrical and configurational parameters for PT and LFR used in the simulations.

Parameter	Unit	Value
Length of steel tube/absorber tube	m	4.06
Length of passive stubs mounted at the end of the manifold	m	0.64
Length of passive stubs mounted at the end of the triples of pipes	m	0.155
Length passive stubs mounted on the central area of the collector	m	0.68
Equivalent length of manifold connections to fixed piping	m	7
Equivalent length of the return pipe	m	21
Number of pipes making up a collector	m	12
Number of collectors making up the loop	-	2
Absorber tube outer diameter	m	0.070
Absorber tube thickness	m	0.003
Glass cover tube diameter	m	0.125
Glass cover tube thickness	m	0.003
Mirror reflectivity	-	0.92
Glass overall transmissivity (normal incidence)	-	0.96
Glass extinction coefficient	-	0.000625
Cermet absorbance	-	0.95
DNI (Direct Normal Irradiance)	W/m^2	800
Ambient temperature	°C	25
Ambient pressure	bar	1
Inlet temperature	°C	225
Inlet pressure	bar	30
Mass flow	kg/s	0.93
Cermet max temperature	°C	600
Loop length	m	100

Table 2. Specific parameters for PT used in the simulations.

Parameter	Unit	Value
Collector width	m	5.9
Collector focal length	m	1.81
Spacing between mirrors	m	1.2

4.1. Optical Model Results

A perfectly aligned parabolic trough with accurate tracking is expected to concentrate nearly all radiation on the receiver's lower half, with the upper half receiving minimal direct sunlight. The optical simulation confirms this expectation. For a perfect system and normal incidence, the fraction of radiation reaching the upper half is minimal (2.38%). However, this fraction increases with the incidence angle, reaching 6.81% at 60°.

Mirror slope errors significantly impact the radiation absorbed by the upper half of the receiver. They also weaken the effect of the incidence angle. For instance, with a standard deviation of 0.2° in mirror slope error, the fraction absorbed in the upper half varies only slightly, from 10.40% (normal incidence) to 11.11% (60° incidence).

An effective slope error of 0.2° is a reasonable estimate (including, e.g., alignment defects among panels, random tracking errors and larger scale deformations due to aging, gravity or thermal effects). As such, realistic operating conditions lead to a non-negligible amount of radiation being absorbed by the upper half of the tube. Moreover, the simulations suggest that a single, representative value can still be used for this fraction across all incidence angles.

A reference case with a standard deviation of 0.2° in mirror slope error and a 30° incidence angle (typical for midday in north–south oriented subtropical systems) was chosen. The figure in Section 5.1 (left) shows the resulting angular distribution of radiation absorbed by the receiver in this scenario.

The glass envelope's absorption distribution closely mirrors the receiver's (within a few percent).

The collector aperture achieves an optical efficiency of 80.86%, with the glass envelope absorbing only 0.066% of the incoming radiation. These percentages, along with the fraction of radiation absorbed by each half of the receiver (10.5% in the upper half), can be considered reasonable approximations across a wide range of incidence angles.

4.2. Thermal Model Results

To validate the theoretical model of the linear parabolic collector, the heat losses calculated through its application were compared with experimental data from the National Renewable Energy Laboratory (NREL) [25]. The laboratory setup uses electric resistors to heat the absorber surface and power transducers to measure the electrical power required to maintain a constant temperature. This power can be considered substantially equal to the heat loss at the same temperature. Data were obtained for absorber temperatures ranging from 50–550 °C at an ambient temperature of 25 °C.

To ensure a reliable comparison, the same collector and receiver geometry were implemented in the heat loss calculation model. To ensure consistent comparisons between calculated and experimental data, the emissivity curve of the cermet coating from [25] was incorporated into the theoretical model.

Figure 5 compares the experimental heat losses reported in [25] with those estimated using the calculation code here developed. The *x*-axis represents the average temperature of the absorber tube's outer surface, considering both halves modeled in the simulation. This comparison shows excellent agreement between the calculation code's results and the experimental heat losses.

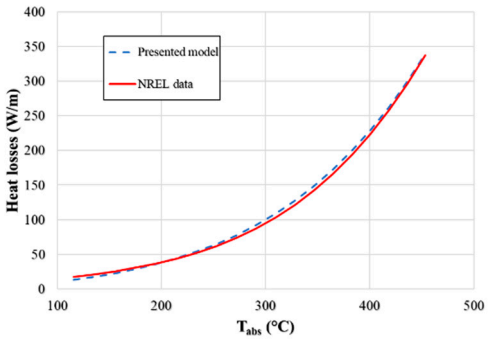

Figure 5. Comparison of the thermal losses measured by NREL [25] and computed by the present model.

Figure 6 presents the simulation results for the solar field's (thermal and fluid-dynamic behavior) as a function of the distance from the inlet section, indicated as x, considering four wind speeds: 0, 2, 6 and 10 m/s.

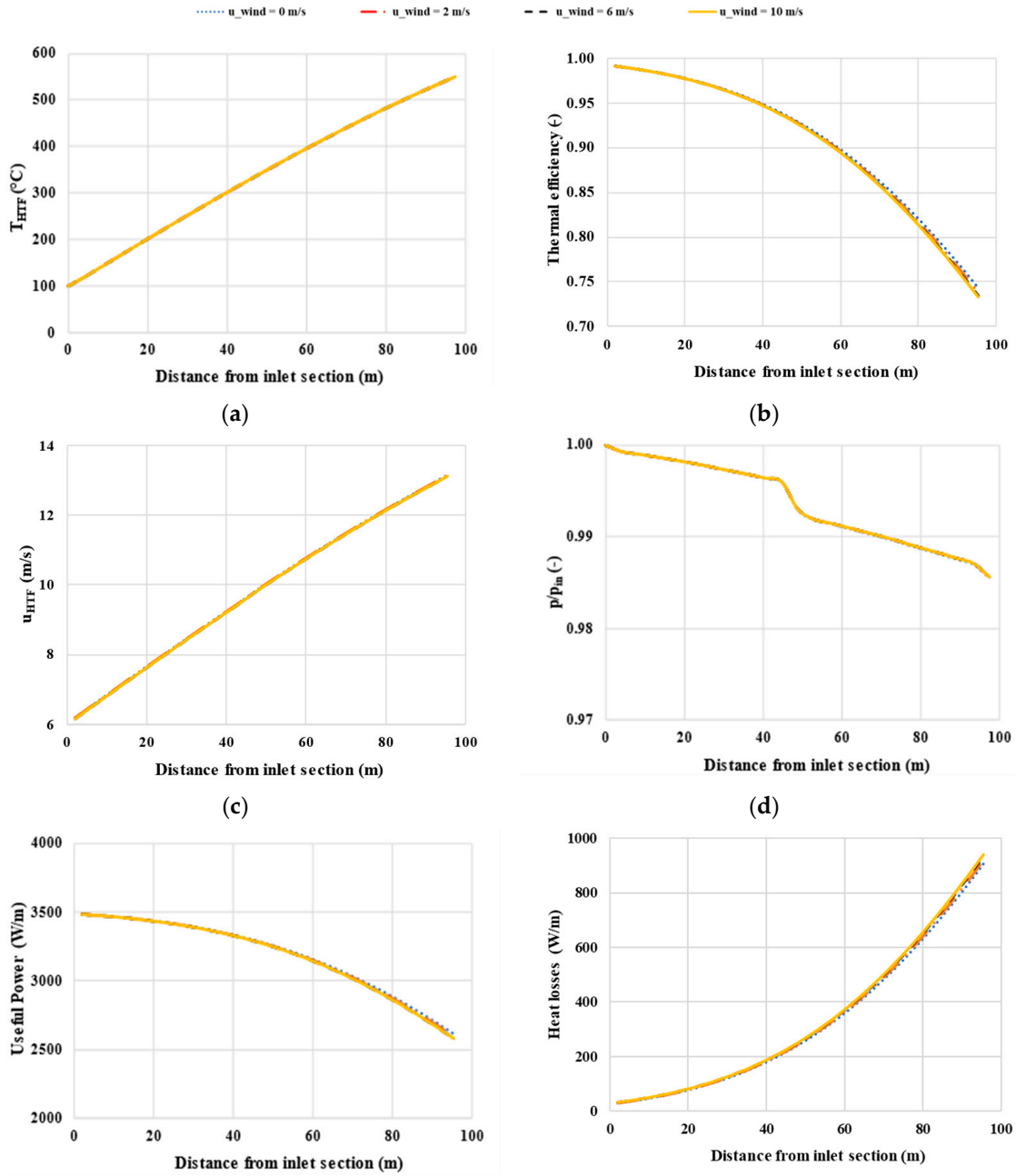

Figure 6. Simulation results as a function of distance from inlet section for Parabolic Trough collector: HTF's temperature (**a**); Thermal efficiency (**b**); HTF's velocity (**c**); HTF's pressure (**d**); useful power collected by HTF (**e**); heat losses from absorber tubes towards environment (**f**).

As expected, the fluid temperature (Figure 6a) exhibits a gradual increase along the collector loop approaching 550 °C, with a maximum temperature for the absorber tube equal to 600 °C. Conversely, the local thermal efficiency (Figure 6b) decreases as the temperature, and consequently the heat loss, rises.

Regarding fluid-dynamic parameters (Figure 6c,d), pressure drops obviously increase as the fluid velocity rises. Additionally, a concentrated pressure drop can be observed in the middle and at the end of the collector. This is likely due to the passive parts of the pipe.

Figure 6f shows that the lost thermal power increases progressively with x, whereas in Figure 6e the useful power decreases as x increases.

The trends observed for all the parameters considered are substantially independent from wind speed variations.

Figure 7 shows the heat losses (convective, radiative and total) as a function of the average absorber tube temperature. In Figure 8 the glass envelope temperatures in the upper and lower part of the linear parabolic collector, and their difference, are plotted against the corresponding average absorber tube temperature. In the following, the main considerations on the obtained results are reported:

- Wind Speed's Impact: Throughout the operating range, convective heat losses increase with wind speed (Figure 7a,b), while radiative losses decrease (Figure 7c,d).
- Temperature Differences: The lower zone experiences higher glass temperatures (Figure 8a,b), and consequently higher losses (Figure 7e,f), compared to the upper zone. This is because it receives a higher portion of incident radiation and maintains a consistently higher average temperature.
- Glass Temperature Gradient: The difference between the lower and upper zone glass temperatures obviously defines the temperature gradient across the glass envelope (Figure 8c). This gradient steadily increases throughout the temperature operating range of the receiver tube and becomes more significant as wind speed decreases.

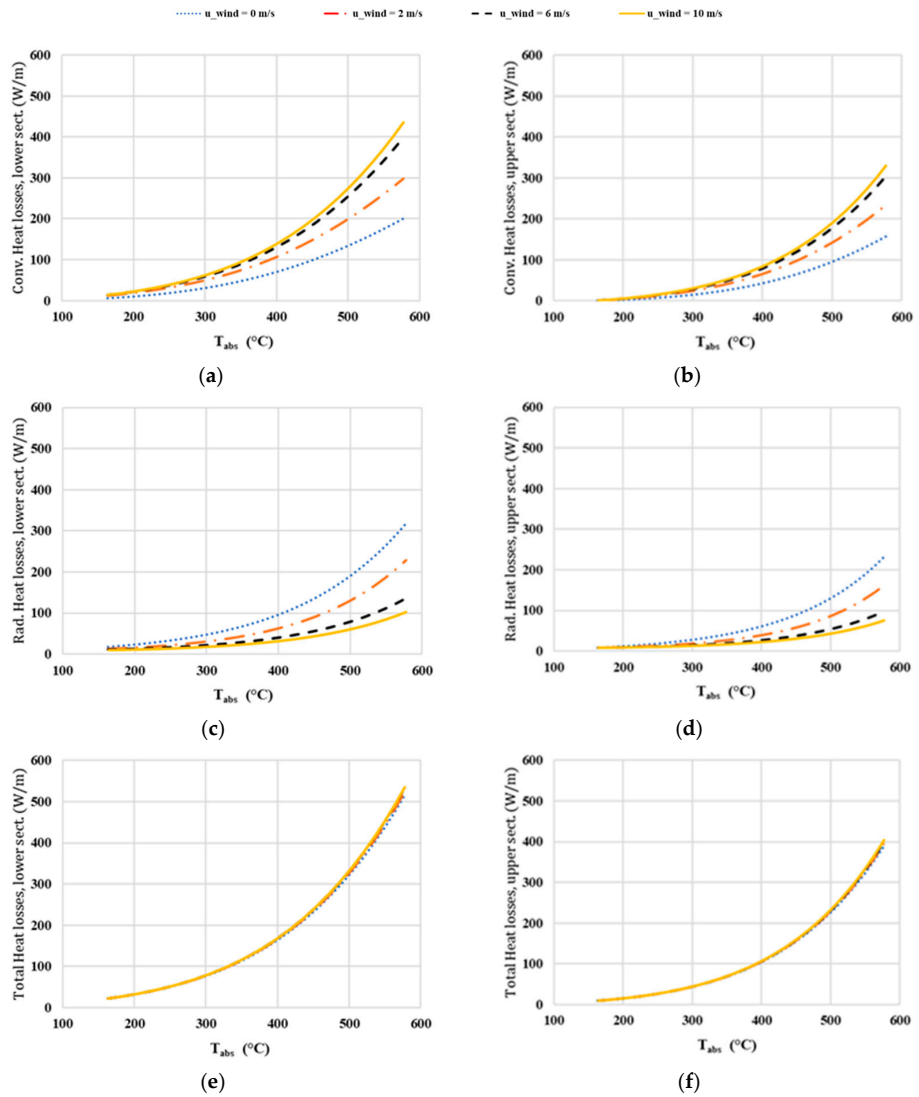

Figure 7. Simulation results: heat losses as function of absorber tube's temperature for the Parabolic Trough collector: convective, lower sector (**a**); convective, upper sector (**b**); radiative, lower sector (**c**); radiative, upper sector (**d**); total, lower sector (**e**); total, upper sector (**f**).

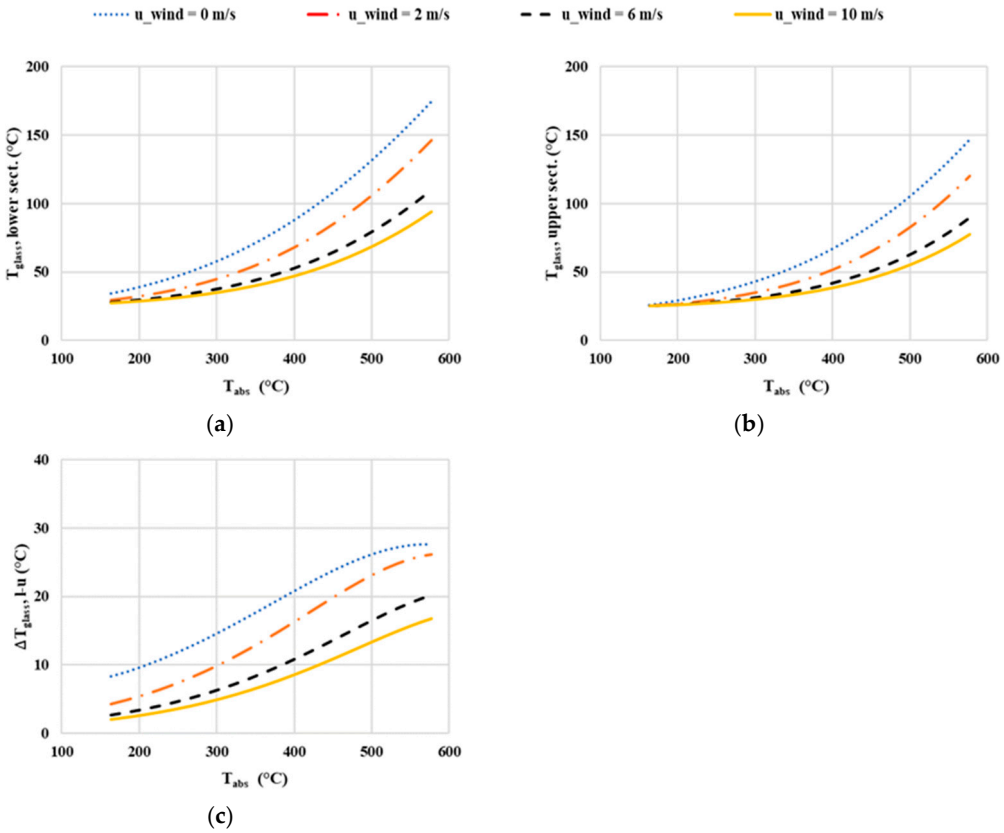

Figure 8. Simulation results: glass envelope's temperatures as function of absorber tube's temperature for the Parabolic Trough collector: lower sector (**a**); upper sector (**b**); difference between lower and upper sector (**c**).

5. Linear Fresnel Model's Application for Thermal Performance Evaluation

The plant's operation was analyzed assuming the same geometrical and configurational collector parameters listed in Table 1, plus the specific LFR parameters shown in Table 3. As mentioned above, a maximum absorber tube temperature of 600 °C was imposed. The specific LFR geometry here considered is derived from a commercial Soltigua product with an evacuated tube receiver, similar to the one described in [26] and illustrated in Figure 9.

Table 3. Specific parameters for LFR used in the simulations.

Parameter	Unit	Value
Number of mirrors	-	10
Mirror width	m	0.625
Spacing factor between mirrors	m	1.2
Receiver height	m	4
Mirror focal length	m	4.617
CPC opening width	m	0.29
CPC opening height	m	3.9375
CPC height	m	0.145
Longer base of the insulating trapezium	m	0.353
Shorter base of the insulating trapezium	m	0.18
Height of the insulating trapezium	m	0.1765

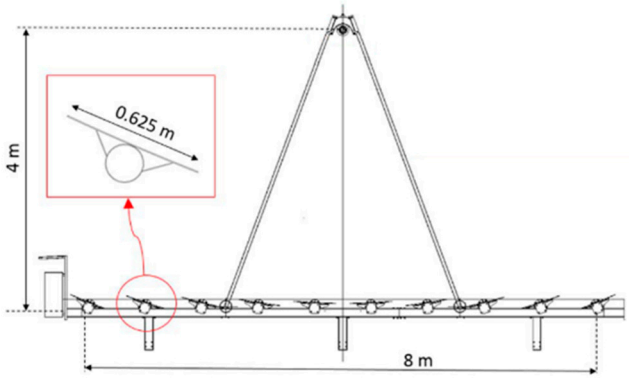

Figure 9. Representation of the LFR geometry used in the model.

5.1. Optical Model Results

The simulations show that the fraction of radiation absorbed by the upper half of the collector tube is relatively insensitive to incidence angles when considering a realistic effective slope error distribution.

For a standard deviation of 0.2° in the effective slope error, the absorption fraction at normal incidence is 25.17%. This value increases slightly to 28.59% for a longitudinal incidence angle of 60° (i.e., along the collector axis) and decreases slightly to 24.20% for a transversal incidence angle of 60° (i.e., perpendicular to the collector axis).

While the dependence on the longitudinal angle is somewhat more pronounced compared to parabolic troughs, using a fixed absorption ratio for the upper half remains a reasonable simplification for thermal simulations. This is especially true considering that a longitudinal angle of 60° is unlikely for a north–south oriented solar plant in a subtropical or tropical region.

Similarly to the parabolic trough analysis, a representative case was chosen with specific incidence angles:

- Longitudinal incidence: 30° (along the collector axis);
- Transversal incidence: 0° (representing solar noon);
- Error standard deviation: 0.2°.

Figure 10 (right) illustrates the resulting distribution of absorbed radiation across the receiver's surface. In this scenario, 25.50% of the radiation is absorbed by the upper half of the collector tube.

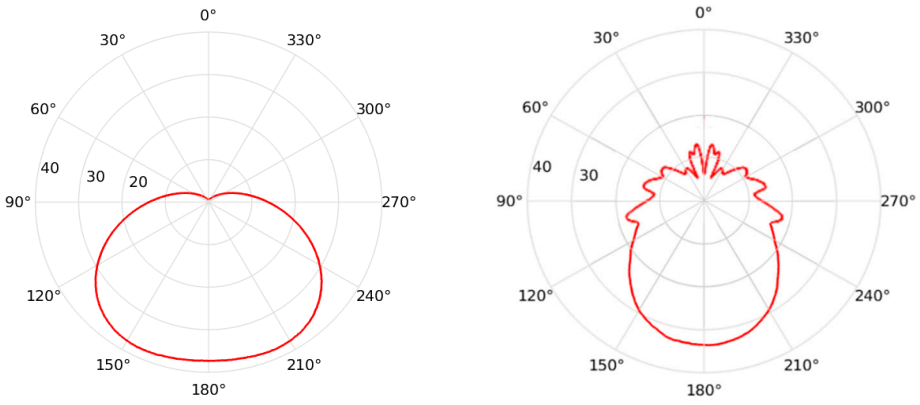

(**a**) (**b**)

Figure 10. Angular distributions of the absorbed radiation on the receiver tube for (**a**) PT and (**b**) LFR.

The overall optical efficiency, considering the incoming radiation on the collector aperture, is 80.09%. The breakdown of the remaining energy is as follows:

- Glass absorption: 0.054%
- Secondary reflector absorption: 3.69%

It is worth noticing that these efficiencies are calculated with respect to the radiation reaching the Fresnel mirrors. This value depends on the specific configuration and needs to be determined for each case by considering the effective collection area of the Fresnel mirrors in their tracking position. For this reason, the computed efficiency results are higher than the optical efficiencies usually reported in the literature for LFR systems.

5.2. Thermal Model Results

To verify the accuracy of the Fresnel solar collector's thermal model, the calculated glass temperatures were compared with data from CFD simulations reported by Reddy et al. [21–23]. Notably, the CFD simulations refer to a Fresnel collector with same geometrical but different optical and thermal properties. The comparison was made on the glass and CPC temperatures calculated for a fixed external surface temperature of the steel absorber half-tube. In the calculations, an absorber temperature of 290 °C and a wind speed range of 0–10 m/s were assumed.

Figure 11 illustrates the comparison between the calculated glass temperatures and those obtained by Reddy et al. [21–23]. The results here obtained tend to overestimate the temperatures with respect to Reddy et al.'s, probably due to the different procedure for the calculation of the radiative losses and to the different convection correlations for the no-wind case. However, this discrepancy becomes less significant as wind speed increases.

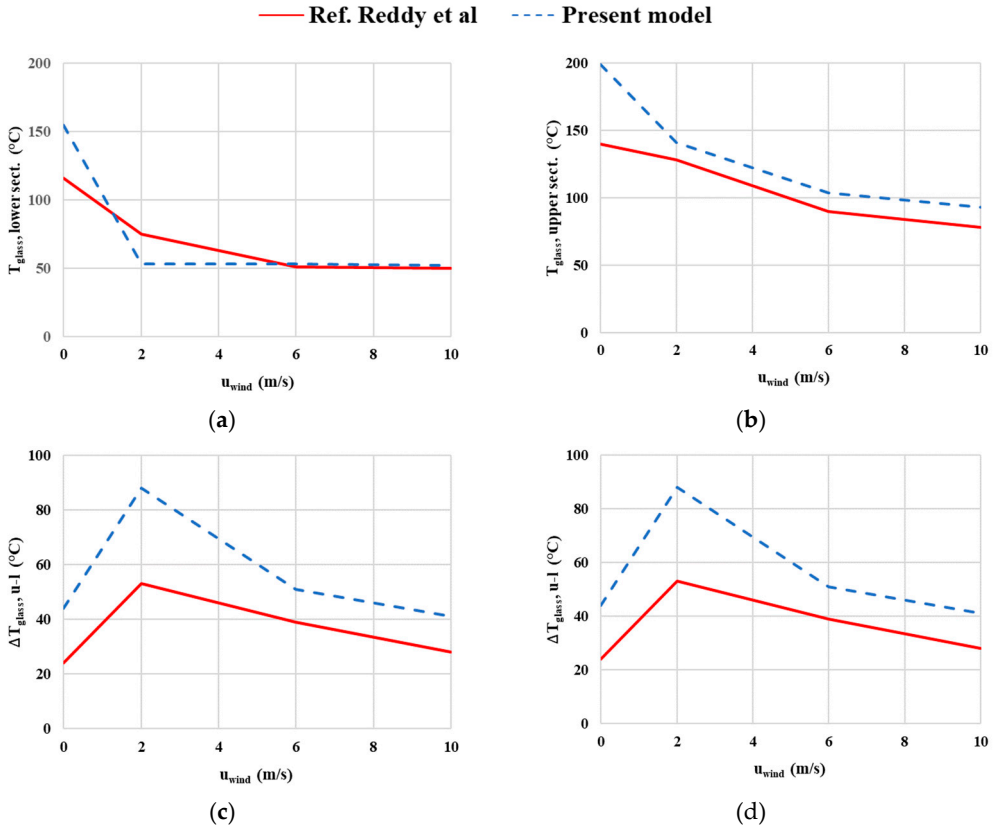

Figure 11. Comparison between the results here obtained and the data from [21–23] for the temperatures of the glass envelope and the CPC, as functions of wind speed for LFR collector: glass envelope's temperature, lower sector (**a**); glass envelope's temperature, upper sector (**b**); difference between upper and lower sector for the glass envelope (**c**); CPC's temperature (**d**).

Simulations results for the Fresnel collector loop are presented in Figure 12, where both thermal and fluid-dynamic variables are shown as functions of x. From Figure 12, the following considerations can be drawn:

- Fluid Temperature and Efficiency (Figure 12a,b): as expected the fluid temperature (Figure 12a) exhibits a gradual increase along the pipe, approaching 550 °C, whereas thermal efficiency (Figure 12b) decreases due to heat losses.
- Fluid-dynamic variables (Figure 12c,d): pressure drops within the collector (Figure 12c,d) proportionally increase with the increase of fluid velocity inside the tube. A concentrated pressure drop is observed in the middle and at the end of the collector.
- Thermal Power (Figure 12e,f): lost thermal power (Figure 12f) shows a progressive increase with x, whereas useful power (Figure 12e) decreases.

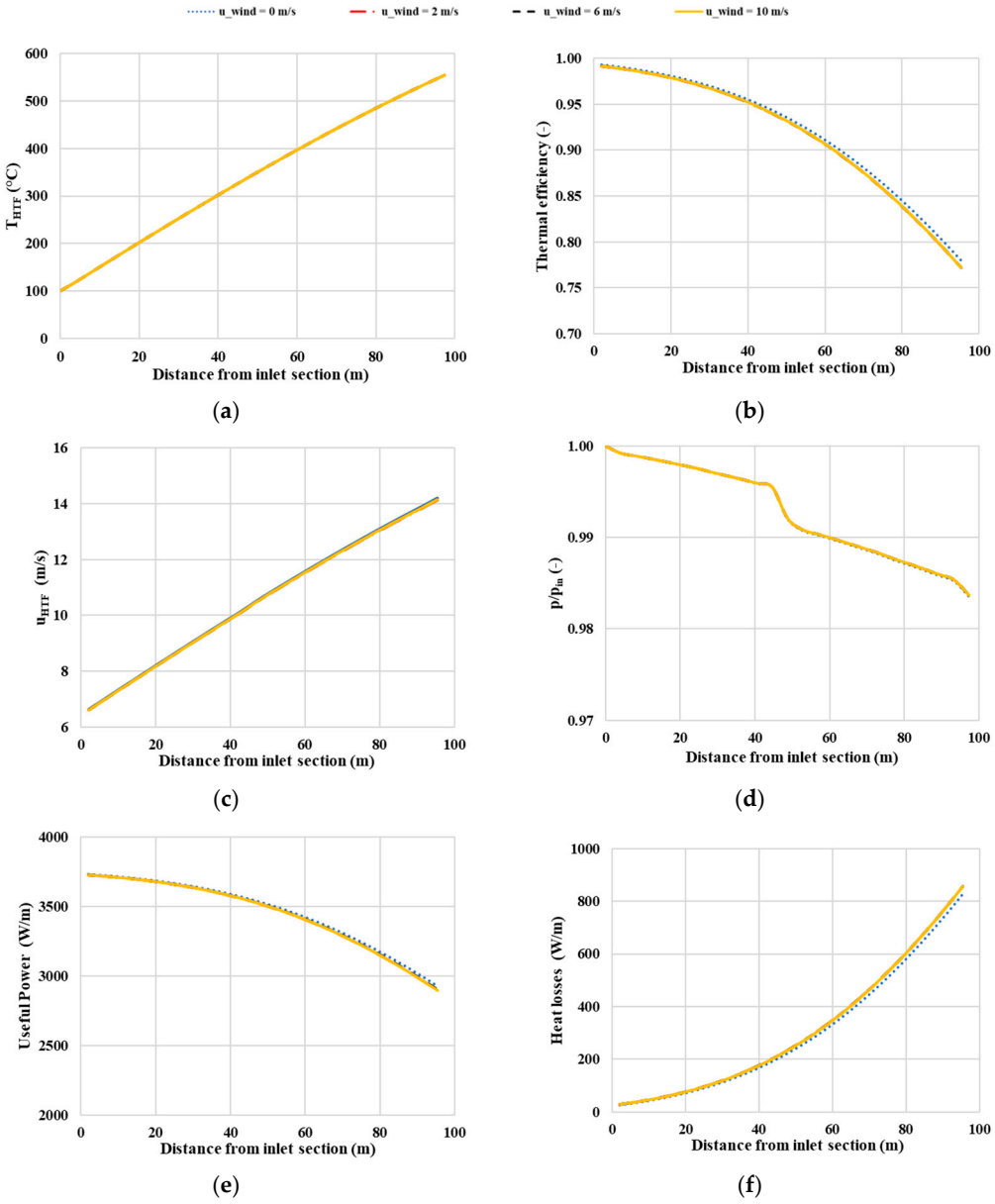

Figure 12. Simulation results as function of distance from inlet section for LFR collector: HTF's temperature (**a**); thermal efficiency (**b**); HTF's velocity (**c**); HTF's pressure (**d**); useful power collected by HTF (**e**); heat losses from absorber tubes towards environment (**f**).

Figure 13 shows the heat losses (convective, radiative and total) as a function of the average absorber tube temperature. Figure 14 shows temperatures of the lower and

upper surfaces of the glass envelope, and CPC temperature as functions of the average temperature of the absorber tube in each zone.

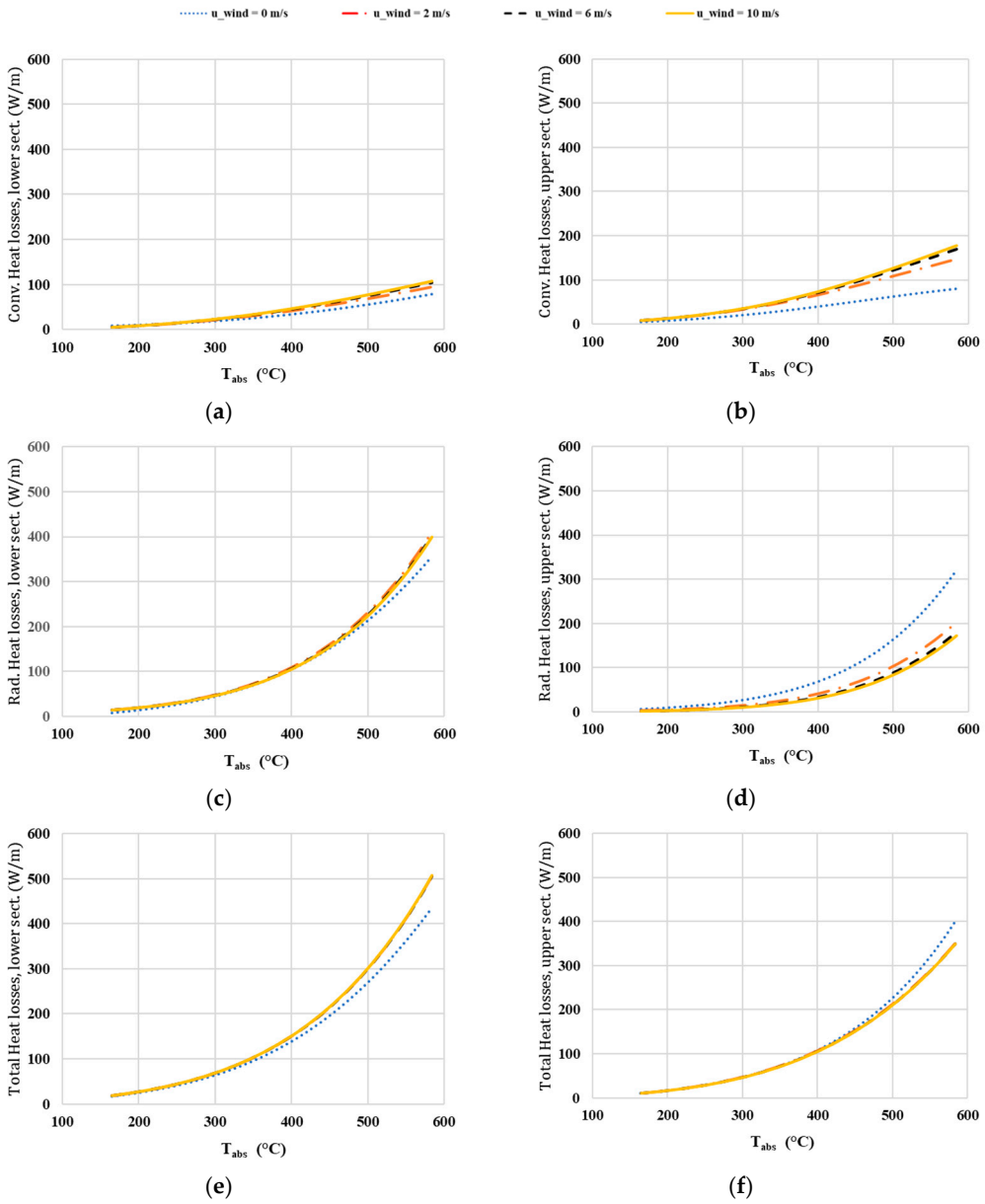

Figure 13. Calculated heat losses as function of absorber tube's temperature for LFR collector: convective, lower sector (**a**); convective, upper sector (**b**); radiative, lower sector (**c**); radiative, upper sector (**d**); total, lower sector (**e**); total, upper sector (**f**).

Qualitatively, the above considerations related to linear parabolic collectors remain valid for Fresnel collectors. It can be noted that, throughout the entire operating temperature range, in the upper zone the convective losses increase with wind speed, while radiative losses decrease (Figure 13b,d). Differently, in the lower section, the heat losses decrease with wind speed (Figure 13a,c). Overall, it can be observed that the total losses in the lower zone are always higher than the losses in the upper part (Figure 13e,f).

Regarding the glass temperatures, it can be observed that the temperature in the upper zone is higher compared to the lower zone (Figure 14a–c). This is due to the "shielding" action of the CPC, which reduces the heat exchange of the upper part of the tube toward the environment (Figure 14d). This temperature difference increases with temperature rise and, in absolute value, has an inverse correlation with wind speed.

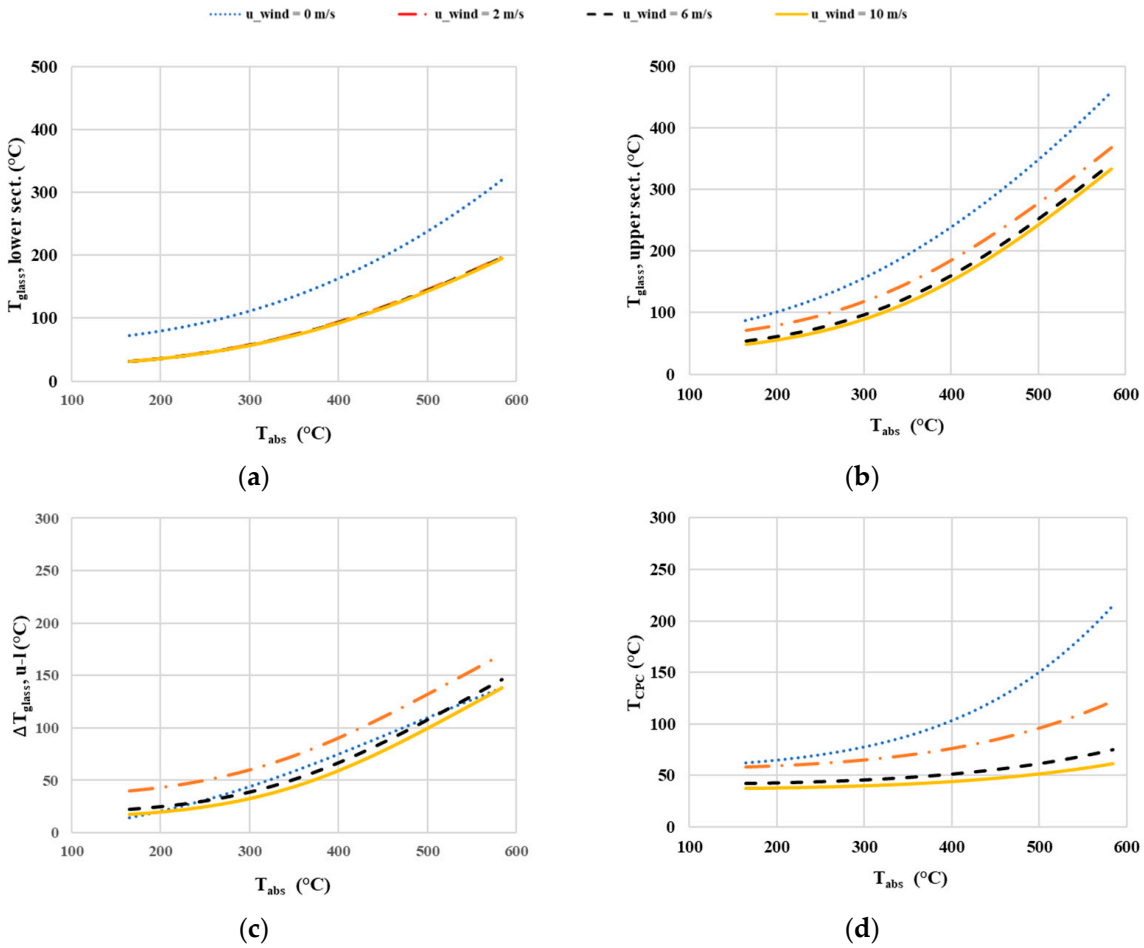

Figure 14. Calculated temperature of the glass envelope and the CPC as function of absorber tube's temperature for Parabolic Trough collector: glass envelope's temperature, lower sector (**a**); glass envelope's temperature, upper sector (**b**); glass envelope's temperature, difference between upper and lower sector (**c**); CPC's temperature (**d**).

6. Discussion

The developed optical–thermal model, which has been validated through comparison with experimental data from the literature, appears to provide realistic temperature estimation of the receiver tube throughout the collector length for both Fresnel and parabolic collectors. This allows the calculation of local heat flows, useful power output, thermal losses and, consequently, the overall collector efficiency. Under the assumptions here considered, the useful power is 310 and 335 kW_{th}, respectively, for PT and LFR collectors, and depending on the actual absorber tube's temperature and wind speed, the thermal efficiency is comprised in the range of 0.733–0.991 for the PT receiver, while it varies from 0.772 to 0.993 for the LFR system. Moreover, the simulations show that, under identical operating conditions, the LFR plant exhibits a lower overall thermal loss than the PT (350 vs. 403 W_{th}/m at a tube receiver temperature of 600 °C). The differences observed in the heat losses are less noticeable in the lower sector of the receiver: they range from 14 to 507 W_{th}/m for LFR collector, while they are in the range of 22–536 W_{th}/m for the PT collector, depending on the actual absorber tube's temperature and wind speed.

The results of thermal efficiency calculation show that, under identical operating conditions, the Fresnel collector exhibits a slightly higher thermal efficiency with respect to the PT: Table 4 reports the thermal efficiency values for both the concentrators, averaging the efficiency calculated over the different wind conditions considered in the simulations. The difference can be attributed to the presence of the secondary reflector (CPC) in the

Fresnel design. The CPC acts as a cavity, reducing convective heat loss and re-radiation to the environment.

Table 4. Comparison between PT and LFR efficiency. Values are averaged on the different wind speed considered.

Collector	Useful Power (kW_{th})	Heat Losses (kW_{th})	Thermal Efficiency (-)
PT	310	32.8	0.904
LFR	335	30.6	0.916

However, the efficiency difference is quite limited (1.2%, on average), and must be weighed against the well-known lower optical efficiency of LFRs with respect to PTs. Is it noteworthy that, for the purposes of this paper, the optical efficiency of the LFR has been computed with respect to the effective collecting area, given a tracking position, but if it was computed with respect to the total mirror area, it could be a 15–30% lower, depending on the LFR's geometry. Moreover, the shielding effect of the CPC does come with a significant drawback: it leads to higher temperatures in the upper (non-irradiated) area of the glass envelope, reaching peaks well above 300 °C in the final part of the collector string. It is worth noticing that the lower part of the glass tube is also affected by the presence of the CPC in the absence of wind, reaching temperatures well above the temperatures obtained for the PT. Additionally, significant thermal gradients exist between the upper (non-irradiated) and lower (irradiated) areas, with a temperature difference that can range from 15 to 170 °C. In contrast, in the case of the PT, the temperature difference between the two sections is small (from 2 to 27 °C). The radial thermal gradients in the case of the LFR can impact the mechanical integrity of the glass, potentially leading to vacuum loss and receiver damage. Furthermore, the large temperature swings can induce significant longitudinal expansions, creating challenges for the glass–metal coupling design.

Nonetheless, it is noteworthy that the results for LFR collector were obtained using a very specific thermal model, whose validity should be experimentally verified: this analysis must be considered as a first approach to identify possible criticalities that should be assessed and thoroughly analyzed when planning a real-life plant, firstly by accurate CFD simulations, and then by experimental tests. Furthermore, the two-halves model surely emphasizes the differences between the two halves of the tubes. For these reasons, it would be premature to discard LFRs as an option, since the fixed collector design offers a significant advantage, particularly when using pressurized HTFs.

The management of a pressurized, high-temperature HTF in a moving receiver appears to be the main drawback in the use of PTs, since the present analysis does not reveal specific criticalities related to thermal stress or low efficiency.

7. Conclusions

This study is focused on the analysis of the technical feasibility of using compressed air as heat transfer fluid in small-scale concentrated solar linear collectors for distributed electricity generation. The work assumes the adoption of readily available components for both linear parabolic trough and Fresnel collectors and the coupling of the solar field with Brayton cycles in a compact and flexible power generation unit.

In the first phase of the analysis, a lumped thermal model using MatLab® software was developed. This model is aimed at estimating the thermal performance of both linear parabolic and Fresnel collectors equipped with evacuated tube receivers using compressed air as a heat transfer fluid. The developed models were validated through the comparison of the simulation results with experimental and literature data.

The analysis shows a high thermal efficiency for both the LFR and PT, with average values above 0.9 (in different wind conditions). This study also evidences a possible critical aspect for the use of LFR collectors with compressed air: the glass covering of the evacuated receiver, under the conditions considered (solar field outlet temperature: 550 °C), reaches

significant temperatures (above 300 °C). Furthermore, due to the presence of the secondary reflector, the temperature difference between the upper and the lower part of the glass envelope can be very high, well above 100 °C in the final part of the collector string. Differently, in the case of the PT, this temperature difference is quite limited (below 30 °C).

It is important to note that these results are based on a simplified model of the receiver tube, based on the tube discretization in only two sections. This modelling approach leads to a discontinuity between the irradiated and non-irradiated surfaces, resulting in a conservative representation of thermal gradients. Future development of this study will introduce a finer discretization of the receiver tube, allowing for a more accurate description of thermal gradients.

Author Contributions: Conceptualization, M.L., V.F. and V.M.; methodology, M.L. and V.F.; software, M.F., M.D. and R.G.; validation, M.F. and M.D.; writing—original draft preparation, R.G., M.F. and M.D.; writing—review and editing, M.D.; supervision, M.D.; project administration, M.L.; funding acquisition, M.L. All authors have read and agreed to the published version of the manuscript.

Funding: This study is supported by the Project funded under the National Recovery and Resilience Plan (NRRP), Mission 4 Component 2 Investment 1.3-Call for tender No. 1561 of 11.10.2022 of Ministero dell'Università e della Ricerca (MUR); funded by the European Union–NextGenerationEU and by Award Number: Project code PE0000021, Concession Decree No. 1561 of 11.10.2022 adopted by Ministero dell'Università e della Ricerca (MUR), CUP-I83C22001800006, Project title "Network 4 Energy Sustainable Transition–NEST".

Data Availability Statement: Data is contained within the article.

Conflicts of Interest: The authors declare no conflicts of interest.

Nomenclature

Abbreviations	
CSP	Concentrated Solar Power
HTF	heat transfer fluid
LFR	Linear Fresnel receiver
PT	Parabolic Trough
Symbols	
c_p	specific heat (W kg^{-1} K^{-1})
d	diameter (m)
$\dot{E}_k$	kinetic energy (W)
h	heat transfer coefficient (W m^{-2} K^{-1})
$\dot{H}$	enthalpy (W)
k	thermal conductivity (W m^{-1} K^{-1})
L_c	characteristic length (m)
Nu	Nusselt number
p	pressure (Pa)
Pr	Prandtl number
$\dot{Q}$	thermal power (W)
$\dot{Q}_{HTF}$	useful power absorbed by HTF (W)
$\dot{Q}_{loss}$	heat losses to environment (W)
r	radius (m)
Ra	Rayleigh number
Re	Reynolds number
T	Temperature (K)
u	fluid velocity (m s^{-1});
v	specific volume (m^3 kg^{-1})
Greek symbols	
α	thermal expansion coefficient (°C^{-1})
ρ	density (kg m^{-3})
μ	dynamic viscosity (Pa s)
Subscripts and superscripts	
1	heat transfer fluid

2	absorber tube inner surface, lower half
3	absorber tube outer surface, lower half
4	glass envelope tube inner surface, lower half
5	glass envelope tube outer surface, lower half
6	absorber tube inner surface, upper half
7	absorber tube outer surface, upper half
8	glass envelope tube inner surface, upper half
9	glass envelope tube outer surface, upper half
10	secondary reflector inner surface
11	secondary reflector outer surface
a	external environment
abs	absorber tube
cond	conductive
conv	convective
eq	equivalent
HTF	heat transfer fluid
i	inner surface
in	collector inlet element
l	lower sector
o	outer surface
out	collector outlet element
rad	radiative
sol,abs	absorbed solar radiation
t	thermal
u	upper sector

References

1. Cabeza, L.F.; Galindo, E.; Prieto, C.; Barraneche, C.; Fernández, A.I. Key performance indicators in thermal energy storage: Survey and assessment. *Renew. Energy* **2015**, *83*, 820–827. [CrossRef]
2. IEA. *Technology Roadmap: Solar Thermal Electricity*, 2014th ed.; International Energy Agency: Paris, France, 2014.
3. Esposito, S.; D'Angelo, A.; Antonaia, A.; Castaldo, A.; Ferrara, M.; Addonizio, M.L.; Guglielmo, A. Optimization procedure and fabrication of highly efficient and thermally stable solar coating for receiver operating at high temperature. *Sol. Energy Mater. Sol. Cells* **2016**, *157*, 429–437. [CrossRef]
4. Falchetta, M.; Gambarotta, A.; Vaja, I.; Cucumo, M.; Manfredi, C. Modelling and Simulation of the Thermo and Fluid Dynamics of the "Archimede Project" Solar Power Station. *Renew. Energy Process. Syst.* **2006**, *3*, 1499–1506.
5. Giaconia, A.; Iaquaniello, G.; Metwally, A.A.; Caputo, G.; Balog, I. Experimental demonstration and analysis of a CSP plant with molten salt heat transfer fluid in parabolic troughs. *Sol. Energy* **2020**, *211*, 622–632. [CrossRef]
6. Liberatore, R.; Giaconia, A.; Petroni, G.; Caputo, G.; Felici, C.; Giovannini, E.; Giorgetti, M.; Branke, R.; Mueller, R.; Karl, M.; et al. Analysis of a procedure for direct charging and melting of solar salts in a 14 MWh thermal energy storage tank. *AIP Conf. Proc.* **2019**, *2126*, 200024.
7. Grena, R.; Tarquini, P. Solar linear Fresnel collector using molten nitrates as heat transfer fluid. *Energy* **2011**, *36*, 1048–1056. [CrossRef]
8. Falchetta, M.; Mazzei, D.; Russo, V.; Campanella, V.A.; Floridia, V.; Schiavo, B.; Venezia, L.; Brunatto, C.; Orlando, R. The Partanna project: A first of a kind plant based on molten salts in LFR collectors. *AIP Conf. Proc.* **2020**, *2303*, 040001.
9. Concentrating Solar Power Projects | NREL. Available online: https://solarpaces.nrel.gov/ (accessed on 12 June 2024).
10. Fernandez-Garcia, A.; Zarza, E.; Valenzuela, L.; Perez, M. Parabolic-trough Solar Collectors and Their Applications. *Renew. Sustain. Energy Rev.* **2010**, *14*, 1695–1721. [CrossRef]
11. Benoit, H.; Spreafico, L.; Gauthier, D.; Flamant, G. Review of Heat Transfer Fluids in Tube-Receivers Used in Concentrating Solar Thermal Systems: Properties and Heat Transfer Coefficients. *Renew. Sust. Energy Rev.* **2016**, *55*, 298–315. [CrossRef]
12. Krishna, Y.; Faizal, M.; Saidur, R.; Ng, K.C.; Aslfattahi, N. State-of-the-art Heat Transfer fluids for Parabolic Trough Collector. *Int. J. Heat Mass Transf.* **2020**, *152*, 119541. [CrossRef]
13. Muñoz-Anton, J.; Biencinto, M.; Zarza, E.; Díez, L.E. Theoretical basis and experimental facility for parabolic trough collectors at high temperature using gas as heat transfer fluid. *Appl. Energy* **2014**, *135*, 373–381. [CrossRef]
14. IEA. *Technology Roadmap: Concentrating Solar Power*, 2010th ed.; International Energy Agency: Paris, France, 2010.
15. Grena, R. Optical simulation of a parabolic solar trough collector. *Int. J. Sust. Energy* **2010**, *29*, 19–36. [CrossRef]
16. Forristall, R. *Heat Transfer Analysis and Modeling of a Parabolic Trough Solar Receiver Implemented in Engineering Equation Solver*; Technical report-OSTI ID: 15004820; U.S. Department of Energy, Office of Scientific and Technical Information: Oak Ridge, TN, USA, 2003.
17. Churchill, S.W.; Chu, H.H.S. Correlating equations for laminar and turbulent free convection from a horizontal cylinder. *Int. J. Heat Mass Transf.* **1975**, *18*, 1049–1053. [CrossRef]
18. Zukauskas, A. Heat transfer from tubes in cross flow. *Adv. Heat Transf.* **1972**, *8*, 93–160.

19. Raithby, G.D.; Hollands, K.G.T. A general method of obtaining approximate solutions to laminar and turbulent free convection problems. *Adv. Heat Transf.* **1975**, *11*, 265–315.
20. Montes, M.J.; Barbero, R.; Abbas, R.; Rovira, A. Performance model and thermal comparison of different alternatives for the Fresnel single-tube receiver. *Appl. Therm. Eng.* **2016**, *104*, 162–175. [CrossRef]
21. Reddy, K.S.; Shanmugapriya, B.; Sundararajan, T. Estimation of heat losses due to wind effects from linear parabolic secondary reflector—Receiver of solar LFR module. *Energy* **2018**, *150*, 410–433. [CrossRef]
22. Reddy, K.S.; Shanmugapriya, B.; Sundararajan, T. Heat loss investigation of 125kWth solar LFR pilot plant with parabolic secondary evacuated receiver for performance improvement. *Int. J. Therm. Sci.* **2018**, *125*, 324–341. [CrossRef]
23. Balaji, S.; Reddy, K.S.; Sundararajan, T. Performance investigation of linear evacuated absorber of 2-stage solar Linear Fresnel Reflector module under non-uniform flux distribution. *Int. J. Low-Carbon Technol.* **2018**, *13*, 92–101.
24. Hilpert, R. Wärmeabgabe von geheizten Drähten und Rohren im Luftstrom. *Forsch. Gebiet Ingenieurw.* **1933**, *4*, 215–224. [CrossRef]
25. Burkholder, F.W.; Kutscher, C.F. *Heat-Loss Testing of Solel's UVAC3 Parabolic Trough Receiver*; Technical report NREL/TP-550-42394; National Renewable Energy Laboratory (NREL): Golden, CO, USA, 2008.
26. Soltigua. *1 MWe CSP-ORC Pilot Plant, Solar Field Process Description*; Report No.: S-F14ET001-M-B-A-2602-C; Soltigua SRL: Gambettola, Italy, 2015.